



Generation of interior cavity noise due to window vibration excited by turbulent flows past a generic side-view mirror

Downloaded from: <https://research.chalmers.se>, 2025-12-04 23:24 UTC

Citation for the original published paper (version of record):

Yao, H., Davidson, L. (2018). Generation of interior cavity noise due to window vibration excited by turbulent flows past a generic side-view mirror. *Physics of Fluids*, 30(3). <http://dx.doi.org/10.1063/1.5008611>

N.B. When citing this work, cite the original published paper.

Generation of interior cavity noise due to window vibration excited by turbulent flows past a generic side-view mirror

Hua-Dong Yao^{a)} and Lars Davidson

Department of Mechanics and Maritime Sciences, Chalmers University of Technology, Gothenburg, Sweden

(Received 8 October 2017; accepted 5 March 2018; published online 23 March 2018)

We investigate the interior noise caused by turbulent flows past a generic side-view mirror. A rectangular glass window is placed downstream of the mirror. The window vibration is excited by the surface pressure fluctuations and emits the interior noise in a cuboid cavity. The turbulent flows are simulated using a compressible large eddy simulation method. The window vibration and interior noise are predicted with a finite element method. The wavenumber-frequency spectra of the surface pressure fluctuations are analyzed. The spectra are identified with some new features that cannot be explained by the Chase model for turbulent boundary layers. The spectra contain a minor hydrodynamic domain in addition to the hydrodynamic domain caused by the main convection of the turbulent boundary layer. The minor domain results from the local convection of the recirculating flow. These domains are formed in bent elliptic shapes. The spanwise expansion of the wake is found causing the bending. Based on the wavenumber-frequency relationships in the spectra, the surface pressure fluctuations are decomposed into hydrodynamic and acoustic components. The acoustic component is more efficient in the generation of the interior noise than the hydrodynamic component. However, the hydrodynamic component is still dominant at low frequencies below approximately 250 Hz since it has low transmission losses near the hydrodynamic critical frequency of the window. The structural modes of the window determine the low-frequency interior tonal noise. The combination of the mode shapes of the window and cavity greatly affects the magnitude distribution of the interior noise. *Published by AIP Publishing.* <https://doi.org/10.1063/1.5008611>

I. INTRODUCTION

Reduction of interior noise is a highly interesting area for automobiles and aircrafts in order to create quiet cabin environments.¹ An important part of the interior noise in cabins is induced by exterior flows.² This problem is emphasized for electric vehicles, in which powertrain noise is greatly reduced by using electric motors instead of engines. However, the generation of the flow-induced interior noise still needs to be systematically explored and understood.²

The generation process of the flow-induced interior noise is illustrated in Fig. 1. The process includes indirect and direct generation. The indirect generation describes the physical mechanism that the exterior hydrodynamic pressure fluctuations excite the structural vibration to emit the interior noise. The hydrodynamic pressure fluctuations arise when the vortices and turbulent boundary layer (TBL) impinge on the structure surface. The direct generation is that the exterior noise causes the structural vibration, which generates the interior noise. The exterior noise is produced by the vortices and TBL due to the fluid compressibility. The hydrodynamic energy in the indirect generation suffers much higher losses than the acoustic energy in the direct generation.^{3,4} However, the acoustic energy is insignificant compared with the hydrodynamic energy, particularly at low Mach numbers. The contributions of the exterior hydrodynamic and acoustic pressure to the interior noise are therefore case-sensitive.⁵

The noise generated from the TBL has been extensively researched.^{6,7} As the surface pressure fluctuations play an important role in the noise generation, their wavenumber-frequency spectra affect the noise spectra.^{8–10} A semi-empirical model for the spectra was proposed by Chase.^{11,12} This model describes the effects of the hydrodynamic and acoustic components that constitute the fluctuating surface pressure. The model was further proven in experiments.^{13,14} Besides, a theoretical model for the spectra of the volume pressure fluctuations was developed based on isotropic turbulence.¹⁵ Lighthill¹⁶ first proposed an acoustic analogy to predict the far-field noise generated by flows in free space. By utilizing modified forms of the acoustic analogy, the TBL noise was predicted on the basis of a hydrodynamic surface pressure model (Ref. 17) or the hydrodynamic velocity and surface pressure obtained from direct numerical simulations (DNSs) (Refs. 6 and 18). Furthermore, DNS of compressible TBL was performed.^{4,19} Their results agree well with the Chase model and experimental data. The interior noise induced by the TBL has been investigated in experiments (Refs. 20 and 21), theoretical models (Refs. 22–24), and simulation of synthetic surface pressure fluctuations (Ref. 25). It has been found in these studies that the acoustic component is important for the interior noise generation.

Side-view mirrors can contribute to significant interior noise in the automobile cabins. The vortices induced by the mirrors produce powerful exterior noise and hydrodynamic impingement,²⁶ which excite the downstream windows. The interior noise can be reduced by suppressing the turbulent

^{a)}Electronic mail: huadong@chalmers.se.

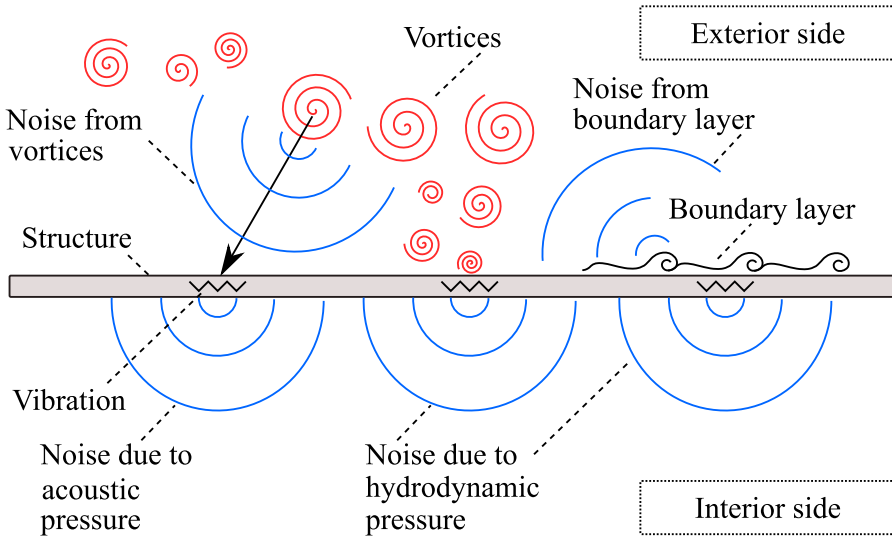


FIG. 1. A schematic diagram of the generation process of the flow-induced interior noise.

flow separation on the mirrors.²⁷ The wavenumber-frequency spectra of the surface pressure fluctuations were studied using compressible flow simulations.²⁸ The spectra were identified to consist of the hydrodynamic and acoustic domains, which are formed by the hydrodynamic and acoustic energy. The domains have a limited overlapping region at low Mach numbers. This characteristic was utilized to separate the hydrodynamic and acoustic components by Hartmann and Ocker.²⁹ It was reported that the acoustic component dominates the interior noise generation.

To simplify real side-view mirrors, a generic mirror was proposed and investigated numerically and experimentally.^{30,31} The surface pressure fluctuations on the plate, on which the mirror is placed, were found dominating the exterior noise generation. The shear layer developed from the mirror side edge was identified to produce powerful hydrodynamic impingement. These findings were verified and elaborated in detail using the incompressible large eddy simulation (LES) and the incompressible detached eddy simulation (DES).³² Furthermore, the wavenumber-frequency spectra for this mirror were analyzed and compared to the theoretical models for the TBL.³³ It was found that the spectra cannot be well described by the models.

It is challenging to conclude the principle physical mechanisms of the interior noise, although some similar phenomena have been presented in the literature as mentioned above. A reason is that the various mirror geometries could introduce different flow characteristics. Moreover, the cabins and windows have different geometries and structural properties, which influence the structural vibration and the efficiencies of the hydrodynamic and acoustic pressure components in the interior noise generation. It is unclear which flow structures are primary noise sources and how the structural vibration is excited efficiently.

This work aims to explore the physical mechanisms of the interior noise generation for the generic side-view mirror. The predominant noise sources will be identified. The wavenumber-frequency spectra will be examined and analyzed based on the local characteristics of the wake. The relation between the noise sources and the interior noise

will be addressed. The influence of the structural characteristics on the interior noise generation and radiation will be clarified. Finally, the efficiencies of the exterior hydrodynamic and acoustic pressure components will be addressed. To avoid approximations introduced by acoustics methodologies (e.g., the acoustic analogy), this study will employ a compressible LES so that the exterior noise is directly computed.

II. GOVERNING EQUATIONS AND COMPUTATIONAL METHODS

A. Method for exterior turbulence and noise

Vibration of glass windows has a limited influence on exterior flows due to its low energy.³⁴ Thus, the structural vibration is neglected in the flow simulation.

The air is assumed as an ideal gas. The compressibility of the air is taken into account. The turbulent flows are simulated using the LES technique. The governing equations with the Favre filter are referred to the original study by Erlebacher *et al.* (Ref. 35) or the authors' study (Ref. 36).

The viscous stress tensors of the sub-grid scales (SGS), τ_{ij} , are modeled using the Smagorinsky model:³⁵

$$\tau_{ij} = \mu_t \left(2\tilde{S}_{ij} - \frac{2}{3}\tilde{S}_{mm}\delta_{ij} \right) - \frac{2}{3}\bar{\rho}k_{sgs}\delta_{ij}, \quad (1)$$

where $\bar{\rho}$ is the filtered density. The strain rate tensors, \tilde{S}_{ij} , are defined as

$$\tilde{S}_{ij} = \frac{1}{2} \left(\frac{\partial \tilde{u}_i}{\partial x_j} + \frac{\partial \tilde{u}_j}{\partial x_i} \right). \quad (2)$$

The kinetic energy of the SGS, k_{sgs} , is given by

$$k_{sgs} = C_I \Delta^2 \tilde{S}_{mn} \tilde{S}_{mn}, \quad (3)$$

where $C_I = 0.0066$. It is a correction factor for the compressibility. Note that τ_{ij} is insensitive to C_I for $Ma_\infty < 0.6$.^{35,37} The filter width, Δ , is determined by the minimum length of

the local grids as $\Delta = \min(\Delta_1, \Delta_2, \Delta_3)$. The dynamic viscosity of the SGS, μ_t , is formulated as

$$\mu_t = C_R \bar{\rho} \Delta^2 \sqrt{\tilde{S}_{mn} \tilde{S}_{mn}}, \quad (4)$$

with $C_R = 0.012$.

The equations are solved using a cell-centered finite volume method.^{38,39} To directly compute acoustic waves, minimal dispersion and dissipation errors are required for the inviscid fluxes that describe the convection.⁴⁰ The discretization of the inviscid fluxes utilizes a low-dissipation third-order upwind scheme.³⁹ Considering mesh grids along a ξ -axis with a uniform grid spacing $\Delta\xi$, the upwind scheme at the i th grid gives

$$\mathbf{q}_i = \begin{cases} \frac{1}{96} (-9\mathbf{q}_{i-3/2} + 59\mathbf{q}_{i-1/2} + 53\mathbf{q}_{i+1/2} - 7\mathbf{q}_{i+3/2}), & \lambda_i > 0, \\ \frac{1}{96} (-7\mathbf{q}_{i-3/2} + 53\mathbf{q}_{i-1/2} + 59\mathbf{q}_{i+1/2} - 9\mathbf{q}_{i+3/2}), & \lambda_i < 0, \end{cases} \quad (5)$$

where $\mathbf{q}_i = [\bar{\rho}_i \ \tilde{u}_{1,i} \ \tilde{u}_{2,i} \ \tilde{u}_{3,i} \ \bar{p}_i]^T$, and the indexes of the neighboring cell centers are $i - 3/2$, $i - 1/2$, $i + 1/2$, and $i + 3/2$. The corresponding characteristic speeds for \mathbf{q}_i are

$$\lambda_i = \begin{cases} 0.5 (\tilde{u}_{j,i-1/2} + \tilde{u}_{j,i+1/2}) s_{j,i} = \lambda_{1,i} \\ \lambda_{1,i} \\ \lambda_{1,i} + 0.5 (c_{i-1/2} + c_{i+1/2}) \sqrt{s_{j,i} s_{j,i}} \\ \lambda_{1,i} - 0.5 (c_{i-1/2} + c_{i+1/2}) \sqrt{s_{j,i} s_{j,i}} \end{cases}, \quad j = 1, 2, 3, \quad (6)$$

where $c_{i\pm 1/2}$ is the speed of sound and $s_{j,i}$ denotes the components of the unit vector along the ξ -axis.

The viscous fluxes are discretized with a second-order central difference scheme to improve the numerical stability.⁴¹ An explicit three-stage second-order Runge-Kutta method is used for the time marching algorithm. The computational solver is an in-house code called G3D.⁴²

B. Method for interior noise

In a vibro-acoustics system, the vibration of the flexible structures is excited by imposing dynamic loads on the surfaces of these structures. Here, the dynamic loads are the exterior surface pressure fluctuations obtained from the flow simulation. The material of the flexible structures is visco-elastic and isotropic. The interior air is considered as a perfect gas.

The modal analysis is performed for the window and cavity separately. Regardless of the damping effect, the natural frequencies (the eigenfrequencies) and the corresponding mode shapes (the eigenvectors) of either the window or the cavity are computed based on the governing equations in the general form,⁴³

$$\mathbf{K}\hat{\mathbf{q}} = \omega^2 \mathbf{M}\hat{\mathbf{q}}, \quad (7)$$

where ω is the angular frequency. The stiffness and mass matrices are depicted as \mathbf{K} and \mathbf{M} , respectively. The definitions of the matrices for the window and the cavity are different. The unknown variable, $\hat{\mathbf{q}}$, is a function of ω . It represents the

structural displacements, $\hat{\mathbf{u}}_S$, for the window, whereas it represents the interior acoustic pressure, $\hat{\mathbf{p}}'_{in}$, for the cavity. The computed mode shapes are normalized to obtain the unit modulus. For the sake of brevity, refer to the detailed derivations and definitions of the matrices in the study by Clough and Penzien.⁴³

The governing equations of the vibro-acoustics system are written as⁴⁴

$$\begin{bmatrix} \mathbf{K}_S + i\omega \mathbf{D}_S - \omega^2 \mathbf{M}_S & \mathbf{C}_{SA} \\ \omega^2 \mathbf{C}_{SA}^T & \mathbf{K}_A + i\omega \mathbf{D}_A - \omega^2 \mathbf{M}_A \end{bmatrix} \begin{pmatrix} \hat{\mathbf{u}}_S \\ \hat{\mathbf{p}}'_{in} \end{pmatrix} = \begin{pmatrix} \hat{\mathbf{p}}'_{ex} \\ 0 \end{pmatrix}, \quad (8)$$

where subscripts S and A denote the window structure and the air, respectively. The term, $\hat{\mathbf{p}}'_{ex}$, denotes the exterior surface pressure fluctuations. The damping matrices are represented by \mathbf{D}_S and \mathbf{D}_A . The matrix, \mathbf{C}_{SA} , is the structural/acoustic coupling matrix. The matrix, \mathbf{C}_{SA}^T , is the transpose of \mathbf{C}_{SA} . The details on the definitions of the vectors and matrices are given in the study by Coyette and Manera.⁴⁴

A finite element method⁴⁵ is used to solve Eqs. (7) and (8) (the software is Actran, produced by Free Field Technologies⁴⁶). The integration in the numerical scheme is optimized to decrease the dispersion error.⁴⁷ A direct multi-frontal massively parallel solver (MUMPS) is utilized for the computation.⁴⁸

III. APPLICATION AND COMPUTATIONAL SETTINGS

A. Configuration

With reference to real automobile cabins, a simple configuration is constructed by assembling the generic side-view mirror,^{30,31} a flat plate with a glass window, and a cavity. A schematic diagram of the configuration is shown in Fig. 2. The settings of the mirror and plate are the same as the experiments,³¹ except for the leading edge of the plate. The corners of the leading edge are of a square shape in the experiments, whereas they are changed to a round shape in the simulation. The change is used to establish a mesh topology aligned with the potential propagation paths of acoustic waves. To model the window, a section of the interface between the plate and cavity is defined as a flexible structure. The noise from the window propagates inside the cavity, which is a classical simple geometry to investigate the interior noise.⁴⁹

The cylindrical part of the mirror has a diameter of $D_{mr} = 0.2$ m. The round leading edge of the plate has a diameter of 1.6 m. The window has a spanwise length of $W_{gw} = 1.2$ m and a streamwise length of $L_{gw} = 1.4$ m. The cavity has a spanwise length of $W_{cv} = 1.4$ m, a streamwise length of $L_{cv} = 1.6$ m, and a height of $H_{cv} = 1.2$ m.

B. Computational settings

1. Settings in flow simulation

Regarding the free-stream conditions, the velocity vector is specified as $\mathbf{u}_\infty = (38.89, 0, 0)$ m/s, the density of the air is $\rho_\infty = 1.198$ kg/m³, the kinematic viscosity is $\nu_\infty = 1.5244 \times 10^{-5}$ m²/s, and the pressure is $p_\infty = 1.01325 \times 10^5$ Pa.

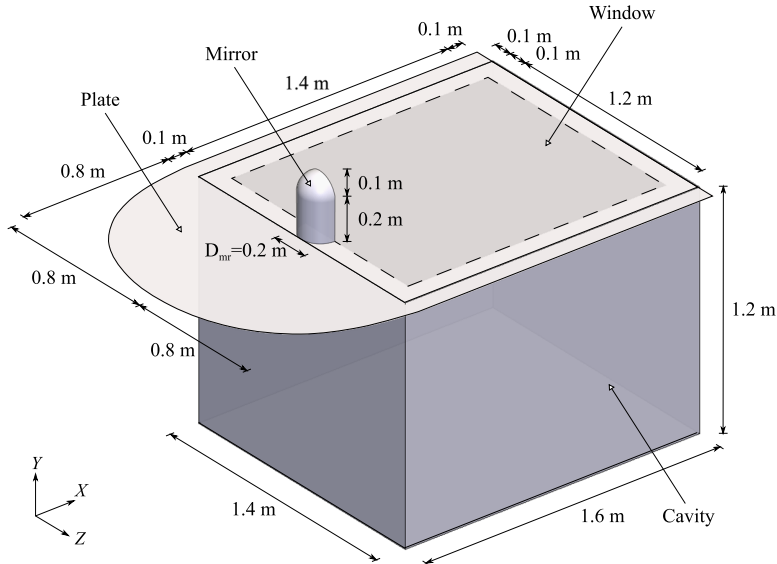


FIG. 2. A schematic diagram of the configuration. The dashed lines mark the window boundaries.

As the exterior noise sources originate from the turbulent flows induced by the mirror and plate, the flow simulation takes into account only these geometries. The computational domain is shown in Fig. 3. The origin of the coordinate system is located at the stagnation point in the connection line between the mirror front face and the plate. The inlet and upper side boundaries are rounded. The bottom boundary is aligned with the plate. The distance between the mirror and the outlet is 6 m, corresponding to $30D_{mr}$, so that the wake vortices at the outlet have sufficiently low energy. The spurious noise created by these vortices can therefore be reduced to a great extent.

The simulation uses a structured mesh that consists of multiple blocks. The topology of the blocks is shown in Fig. 3. The grids on the mirror front face and in the plane of $z = 0$ m are illustrated in Fig. 4. The mesh is refined near the mirror edge with $\Delta x = 1 \times 10^{-4}$ m and $\Delta r < 4 \times 10^{-3}$ m, where Δr represents the cell lengths along the edge. Another refinement is made in the region from the mirror back face

to $x = 0.5$ m, where the vortex shedding initiates and develops. This refined region has $\Delta x < 4 \times 10^{-3}$ m, $\Delta y < 2.6 \times 10^{-3}$ m, and $\Delta z < 2 \times 10^{-3}$ m. In the further downstream region of $0.5 \text{ m} < x < 1.6 \text{ m}$, the cell sizes increase up to $(\Delta x, \Delta y, \Delta z) = (4 \times 10^{-3}, 2.8 \times 10^{-3}, 2.6 \times 10^{-3})$ m. Near the far-field boundaries, the largest cell lengths are $(\Delta x, \Delta y, \Delta z) = (9.22 \times 10^{-2}, 6.28 \times 10^{-2}, 9.74 \times 10^{-2})$ m. The first-layer cells near the plate have a fixed height of 2×10^{-5} m. To ensure smooth cell scale transition, the cell growth rates are globally controlled below 1.15. Particularly, the growth rates of the boundary layer cells near the mirror are limited between 1.03 and 1.07, and those near the plate are set to 1.1. The total number of the nodes is 3.54×10^7 . The time step interval is $\Delta t = 4 \times 10^{-8}$ s, to ensure the numerical stability.

The non-reflective boundary condition is specified on the side and bottom boundaries, the inlet, and the outlet.⁵⁰ The no-slip condition is set on the walls of the mirror and plate. The walls are adiabatic.

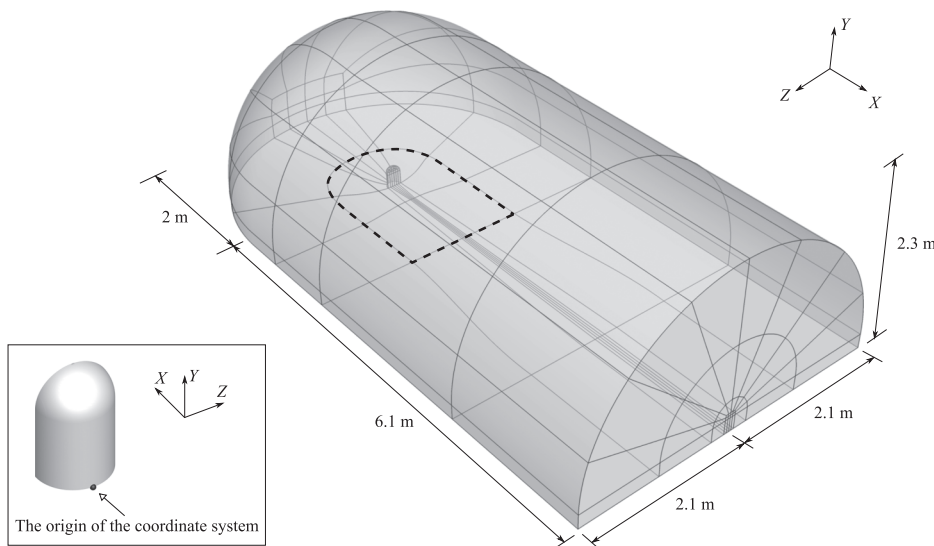


FIG. 3. The computational domain in the flow simulation, where the lengths from the boundaries to the origin of the coordinate system are labeled. The dashed lines mark the plate boundaries. The solid lines show the topology that is used to split the domain into multiple blocks for the structured mesh generation.

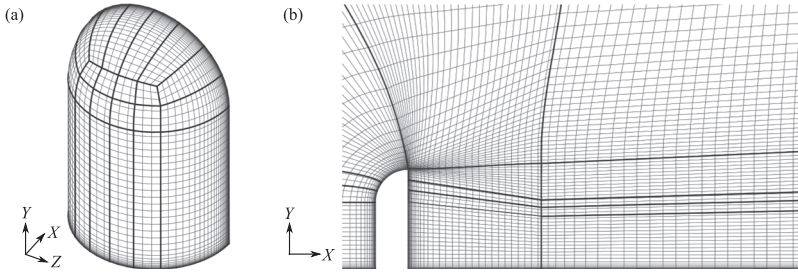


FIG. 4. The grid lines of the mesh (a) on the front face of the mirror and (b) $z = 0$ m. Each of the 5th grid lines is shown. The bold lines mark the bounds of the mesh blocks.

The simulation is converged to achieve a statistically stationary solution before extracting the flow quantities for the acoustic analysis. The exterior pressure fluctuations are defined as $p'_{ex} = p_{ex} - \langle p_{ex} \rangle$, where p_{ex} is the exterior pressure, and the angle bracket represents the time-averaged operator.

2. Settings in vibro-acoustics simulation

The density of the glass, ρ_{gw} , is 2.5×10^3 kg/m³. The Young's modulus of the glass, E_{gw} , is 6×10^{10} Pa. The loss factor of the glass, η_{gw} , is set to 0.02. It is worth noting that a loss factor in the real world is frequency-dependent.⁵¹ To validate the present assumption, a parametric study is performed in Appendix A. The Poisson ratio, μ_{gw} , is 0.23. The window thickness, h_{gw} , is 4×10^{-3} m. The density of the air, ρ_{cv} , is set as 1.225 kg/m³. The speed of sound is $c_{cv} = 340$ m/s. The decay coefficient of wave amplitudes due to the air viscosity is specified as $\mu_{cv} = 5 \times 10^{-4} \omega / c_{cv}$,⁵² where ω denotes the angular frequency. Note that a real decay coefficient for acoustic waves in the air does not linearly vary with frequencies. A classical absorption scales with f^2 .⁵³ The current setting will not influence the results but limit the amplitudes of the resonance modes in the cavity. The reference pressure is $p_{ref} = 2 \times 10^{-5}$ Pa.

A structured mesh with uniform quadrangle elements is generated for the window. The element size, Δ_e , is 0.0125 m. The elements in the cavity mesh are hexahedrons with a uniform size of 0.025 m. The grid lines of the window mesh are aligned with those of the cavity mesh. The maximum resolved frequency is derived according to $f_{max} = c_{cv} / (n_e \Delta_e)$, where n_e is the number of elements per wavelength. For a linear analysis with the finite element method, $n_e = 6$ is suggested.⁵⁴ Therefore, f_{max} is approximately 4533 Hz for the window and 2266 Hz for the cavity. In the following analysis, the results are presented up to 4000 Hz although those at high-frequencies are not well predicted due to the resolution. The minimum frequency resolved is 5 Hz, which is determined based on the duration of the exterior fluctuating pressure signals.

The window edges are fixed without displacements and rotations. The cavity walls are imposed with a specular wall boundary condition that does not introduce an absorption effect into the reflection of the noise.

In the coupling method, the flow simulation is first performed to obtain the surface pressure fluctuations on the window. The pressure data are collected every 1×10^{-5} s. To pass the data on to the vibro-acoustics simulation, the data are transformed from time to frequency using the fast Fourier transform (FFT) since the vibro-acoustics solver is implemented in the frequency domain.

A conservative interpolation approach with the second-order accuracy in space is used to map the data from the flow grids to the vibro-acoustics grids.⁵⁵

IV. RESULTS AND DISCUSSION

A. Validation of flow simulation

The mesh resolution near the plate is examined in terms of Δy^+ of the first-layer cells. The values are smaller than 1.3. For the sake of brevity, contours of Δy^+ are not presented. There are at least three grid points in $0 < y^+ < 10$ so that the inner layer is directly resolved. According to the study by Wollblad *et al.*,³⁹ the Smagorinsky model with the current parameters of C_R and C_I can introduce limited dissipation near a wall if $\Delta y^+ \approx 1$, as compared with the wall-adapting local eddy-viscosity (WALE) model. A damping function near the walls is therefore not applied to the simulation.

The time-averaged exterior pressure coefficient is defined as $\langle C_p \rangle = (\langle p_{ex} \rangle - p_{\infty}) / (0.5 \rho_{\infty} U_{\infty}^2)$, where U_{∞} is the stream-wise free-stream velocity. In Table I, $\langle C_p \rangle$ obtained from the present simulation are compared with the experiments (Refs. 30 and 31) and the incompressible LES and DES (Ref. 32). The results of the compressible LES are closer to the experimental data than the other numerical methods, except for the overestimated value at the sensor S5. This overestimation is also reported by Höld *et al.*³¹

TABLE I. The time-averaged pressure coefficients, $\langle C_p \rangle$, at several sensors on the mirror surfaces. The sensor locations are documented in Appendix B.

	S5	S10	S15	S20	S25	S30	S34
Experiments ^{30,31}	-0.629	-0.725	0.886	0.991	-0.753	-0.507	-0.484
Present compressible LES	-0.457	-0.592	0.879	0.991	-0.557	-0.498	-0.472
Incompressible DES ³²	-0.668	-0.896	0.866	0.956	-1.112	-0.453	-0.451
Incompressible LES ³²	-0.727	-0.898	0.898	0.1	-1.102	-0.477	-0.443

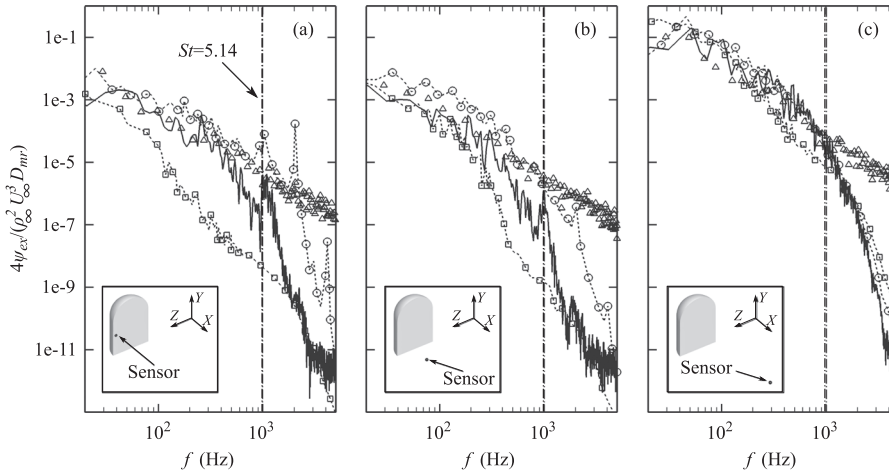


FIG. 5. The normalized PSDs of the exterior surface pressure fluctuations at the sensors (a) near the mirror edge, with the coordinates of $(x, y, z) = (0.1, 0.117, 0.085)$ m; (b) in the region impinged by the recirculation bubble, $(x, y, z) = (0.2, 0, 0)$ m; and (c) in the region impinged by the side shear layer, $(x, y, z) = (0.498, 0, -0.142)$ m. The compressible LES is shown by —, the experiments^{30,31} by Δ , the incompressible LES³² by $\cdots\circ\cdots$, and the incompressible DES³² by $\cdots\square\cdots$. The sensor locations are illustrated in the insets.

The one-sided power spectral density (PSD) of p'_{ex} is denoted by ψ_{ex} . In the computation of the PSD in this study, the time samples are divided into four segments with the same length and 50% overlapping. The formulation of ψ_{ex} and the signal-processing approach are given in Appendix C.

The normalized PSDs, $\psi_{ex} / (0.25 \rho_\infty^2 U_\infty^3 D_{mr})$, of the different methods are shown in Fig. 5. The results are presented in narrow bandwidths. At the sensor near the mirror edge, the compressible and incompressible LES results exhibit local peaks at 1000 Hz corresponding to the Strouhal number of $St = 5.14$. Here, $St = f D_{mr} / U_\infty$. In addition, the incompressible LES shows obvious local peaks at 2000 Hz and 3000 Hz. These peaks are caused by energetic coherent structures in the free shear layer that develops from the mirror edge. At the sensor in the surface region impinged by the recirculation bubble in Fig. 5(b), the compressible LES captures peaks at 1000 Hz and 2000 Hz.

The current results commonly present a glaring discrepancy above 1000 Hz in comparison with the experimental data, as displayed in Fig. 5. A reason is that the mesh resolution is not sufficient to capture the high-frequency content. The cutoff frequency is estimated based on $f_{\max} = \sqrt{2 \langle k_{ex} \rangle / 3} / (2 \Delta_c)$, where $\langle k_{ex} \rangle$ is the time-averaged turbulence kinetic energy and Δ_c denotes the length scale of a cell defined as $\Delta_c = \max(\Delta x, \Delta y, \Delta z)$. Regarding $\Delta_c = 4 \times 10^{-3}$ m near the walls, the cutoff frequencies at the three sensors are 583 Hz, 684 Hz, and 1314 Hz. While this indicates that there is an

issue in fully capturing the physics at the smaller length scales, these cutoff frequencies are comparable with the most energetic modes of the cavity, which are at low frequencies, as discussed in the subsequent analysis.

A mesh sensitivity study for the compressible LES has been conducted using three meshes including the present mesh, which has the finest resolution. The meshes are generated by refining the resolution with factors of 0.8 for Δx , 0.9 for Δy , and 0.95 for Δz . Since the simulation method uses the implicit filtering, the solution is dependent on the resolution. However, it has been observed that all the meshes give consistent PSDs below the cutoff frequencies of the coarsest mesh as well as consistent $\langle C_p \rangle$. For the sake of brevity, only the results of the finest mesh are presented.

The incompressible LES shows the best agreement with the experimental data in Fig. 5, although the resolution of its mesh is comparable to that of the coarsest mesh in the compressible LES. The dynamic Smagorinsky model⁵⁶ is used in the incompressible LES. It is therefore believed that the underestimated PSDs of the compressible LES may be caused by the static Smagorinsky model, which is known to introduce extra dissipation.⁵⁷

B. Characteristics of flow field

To identify the local features of the wake, streamlines of the time-averaged velocity field are illustrated in Fig. 6.

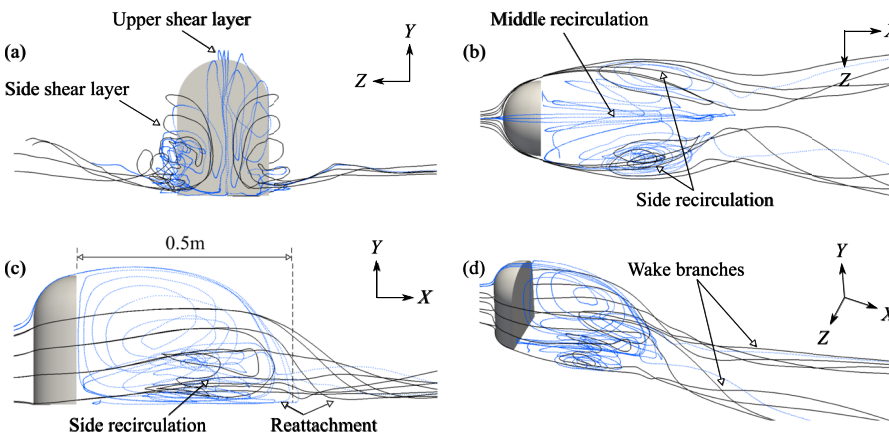


FIG. 6. Streamlines of the time-averaged velocity field from different views. Streamlines from the upper edge of the mirror are colored in blue, and those from the side edge are colored in black.

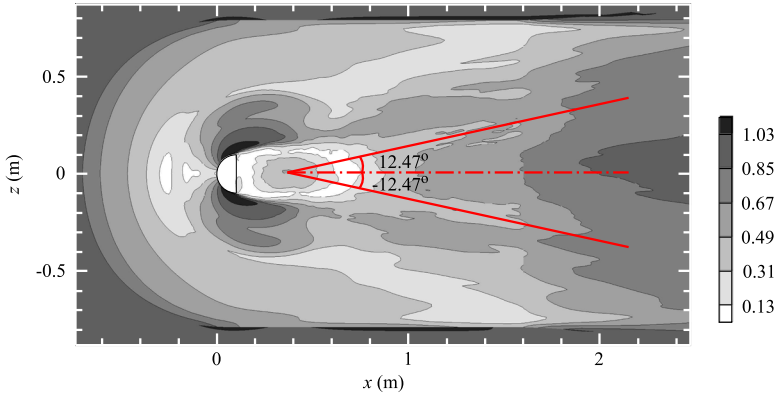


FIG. 7. Contours of the normalized time-averaged velocity magnitudes, $|\langle \mathbf{u}_{ex} \rangle|/U_\infty$, in the plane of $y = 2 \times 10^{-3}$ m. The vertex of the angles is located at $(x, z) = (0.37, 0.01)$ m.

Three main regions are observed: a free shear layer, a recirculation bubble, and two far-downstream wake branches. The free shear layer initiates from the mirror edge and triggers the recirculation bubble. At a distance of 0.5 m (corresponding to $2.5D_{mr}$) downstream of the mirror, the upper shear layer reattaches to the plate. This distance is roughly measured at the end of the recirculation bubble in the plane of symmetry. The wake branches are formed downstream of the recirculation bubble. Large hydrodynamic surface pressure can be generated on the window due to the impingement from the main wake regions.³² A potential consequence is that the flow structures in the regions could become predominant indirect noise sources.

To study the convection effect, the normalized time-averaged velocity magnitudes, $|\langle \mathbf{u}_{ex} \rangle|/U_\infty$, in the plane of $y = 2 \times 10^{-3}$ m are shown in Fig. 7. The wake branches are identified with the convective expansion angles of $\alpha_c = \pm 12.47^\circ$. As a local minimum magnitude is found at $(x, z) = (0.37, 0.01)$ m, this position is appointed as the vertex of the convection expansion angle. The z -coordinate of the vertex is not 0 m since the contours are not exactly symmetric. The non-zero expansion angles indicate that the main convection has a spanwise component. This feature is different from the TBL, where the expansion angle is 0° .

C. Wavenumber-frequency spectra of surface pressure fluctuations

The hydrodynamic and acoustic pressure fluctuations follow the different wavenumber-frequency relationships. This

can be addressed based on the normalized wavenumber-frequency spectra, χ_{ex} , for p'_{ex} on the window. The formulation of χ_{ex} is presented in Appendix C. Considering the main convection with the convective expansion angles of $\alpha_c = \pm 12.47^\circ$ in Fig. 7, the spectra at $k_z/k_x = \tan(\alpha_c)$ are studied to identify the relationships. Define the spectra as

$$\chi_c(k_c, \omega) = \sum_{\alpha_c = \pm 12.47^\circ} \chi_{ex}(k_c \cos(\alpha_c), k_c \sin(\alpha_c), \omega). \quad (9)$$

Contours of χ_c are illustrated in Fig. 8. Three local domains with intensive energy are discerned. The major domain of a large size is distributed approximately along a phase velocity of $\omega/k_c = 0.6U_\infty$, corresponding to U_c (the main convection velocity). The phase velocity of the minor domain of a large size is found as $-U_c$. It indicates the local convection velocity introduced by the recirculating flow. Moreover, the smallest domain is observed to follow the phase velocity of $c_\infty + U_\infty$, where c_∞ denotes the speed of sound of 340 m/s. The phase velocity is related to the speed of the acoustic waves propagating downstream in the main flow. Note that part of the smallest domain should follow the phase velocity of $-c_\infty + U_\infty$, which is contributed by the acoustic waves propagating upstream. However, this is difficult to detect due to the low magnitudes. This phenomenon was also reported by Gloerfelt and Berland⁴ in the investigation of the TBL noise at the Mach number of 0.5.

Contours of χ_{ex} at several frequencies are shown in Fig. 9. The local domains, which are identified in Fig. 8 based on the wavenumber-frequency relationships, are approximately

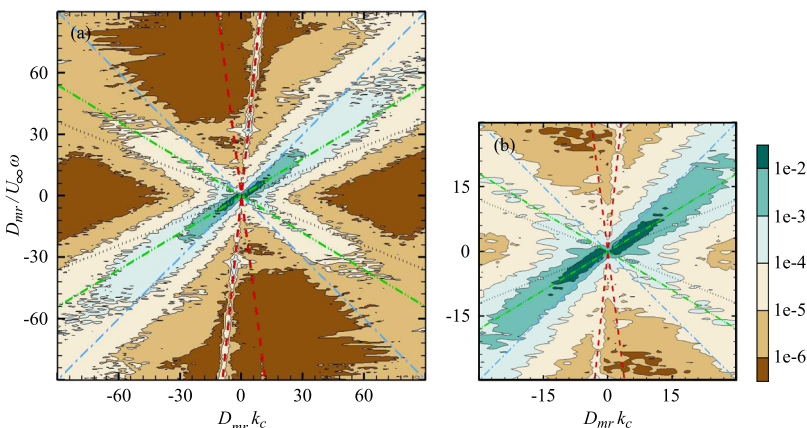


FIG. 8. (a) Contours of χ_c and (b) the zoomed contours. The characteristic phase velocity of ω/k_c : --- (red), $\pm c_\infty + U_\infty$; - · - (blue), $\pm U_\infty$; - · · - (green), $\pm 0.6U_\infty$; · · · · (black), $\pm 0.4U_\infty$.

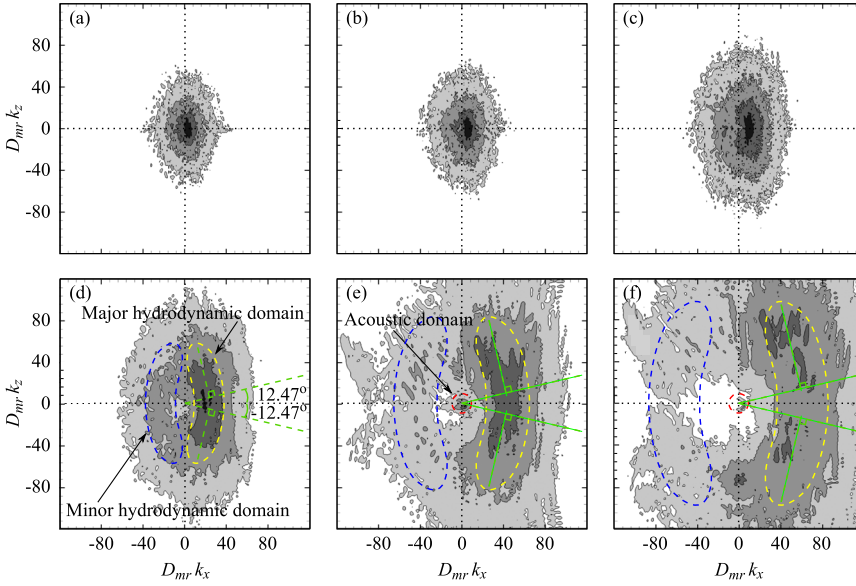


FIG. 9. Contours of the normalized wavenumber-frequency spectra, χ_{ex} , at (a) 50 Hz, (b) 100 Hz, (c) 200 Hz, (d) 500 Hz, (e) 1000 Hz, and (f) 1500 Hz. The contour levels from white to black are 1×10^{-6} , 1×10^{-5} , 1×10^{-4} , and 1×10^{-3} . The convective expansion angles are $\alpha_c = \pm 12.47^\circ$.

marked out in the contours. According to the Chase model, the major domain results from the hydrodynamic pressure fluctuations that are convected by the main flow. The smallest domain surrounding the origin above 500 Hz is produced by the exterior noise. However, the model cannot explain that there is an additional minor domain and that the major and minor domains are distributed in bent elliptic shapes. The reasons for these new features are the specific characteristics of the wake, which do not exist in the TBL. Since the wake contains the recirculating flow as shown in Fig. 6, the convection of a negative velocity is introduced to the hydrodynamic pressure fluctuations. The convection leads to the additional minor domain. Furthermore, the spanwise main convection is found in Fig. 7. As a result, the hydrodynamic domains become bent with α_c . The bending effect is also reported by Caro *et al.*³³

D. Decomposition of exterior surface pressure fluctuations

As explained above for Figs. 8 and 9, the hydrodynamic and acoustic pressure components have intensive energy in the different domains in the wavenumber-frequency spectra. This feature can be taken to approximately decompose the

surface pressure fluctuations into the hydrodynamic and acoustic components, denoted by $p'_{ex,hy}$ and $p'_{ex,ac}$, respectively.²⁹

As observed in Fig. 8, the acoustic energy spreads in a narrow region, where the phase velocity can deviate from $c_\infty + U_\infty$. This phenomenon suggests that the propagation of the acoustic waves can be slightly affected by the convection of the turbulent flows in addition to the mean free-stream flow. The turbulent-flow convection affects both hydrodynamic and acoustic pressure fluctuations. Moreover, Fig. 8 shows that the phase velocity of the hydrodynamic domains, which is caused by the turbulent-flow convection, can vary from negative values to large positive values (e.g., $1.5U_\infty$). A schematic diagram of the wavenumber-frequency spectra at ω as a function of wavenumbers, k_r , is illustrated in Fig. 10. Here, the wavenumber vectors of the spectra are given by $\mathbf{k} = k_r(\cos \alpha, \sin \alpha)$ with fixed α . The unit vector along the k_r -axis is defined as $\mathbf{a} = (\cos \alpha, \sin \alpha)$. A parameter, Δu , is introduced to quantify the phase velocity range between $u_\infty \cdot \mathbf{a} - \Delta u$ and $u_\infty \cdot \mathbf{a} + \Delta u$, which should involve most of the effective turbulent-flow convection. Thus, acoustic waves propagate upstream with the negative phase velocity below $-c_\infty + u_\infty \cdot \mathbf{a} + \Delta u$ and propagate downstream with the positive phase velocity above $c_\infty + u_\infty \cdot \mathbf{a} - \Delta u$. The dominant acoustic energy is included

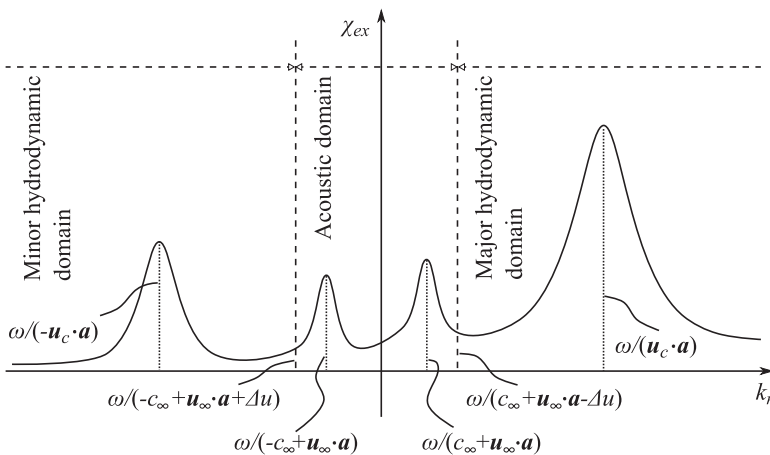


FIG. 10. A schematic diagram for the wavenumber-frequency spectra at ω as a function of k_r , where \mathbf{a} is the unit vector along the k_r -axis.

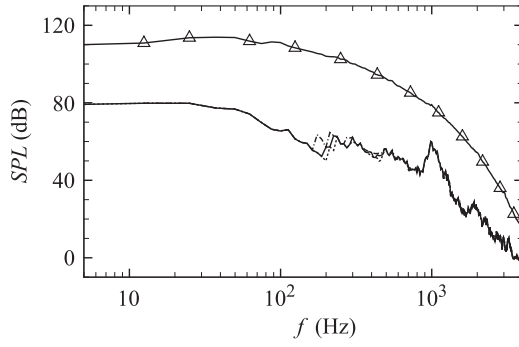


FIG. 11. The space-averaged SPLs: Δ , p'_{ex} ; \cdots , $p'_{ex,ac}$ ($\Delta u = 0.5U_\infty$); — , $p'_{ex,ac}$ ($\Delta u = U_\infty$); $-\cdot-$, $p'_{ex,ac}$ ($\Delta u = 1.5U_\infty$).

in the wavenumber range between $\omega/(-c_\infty + \mathbf{u}_\infty \cdot \mathbf{a} + \Delta u)$ and $\omega/(c_\infty + \mathbf{u}_\infty \cdot \mathbf{a} - \Delta u)$.

According to the wavenumber-frequency relationships, it is considered that the exterior acoustic component is formed by the energy inside the acoustic domain, as shown in Fig. 10. This component is thus formulated as

$$p'_{ex,ac}(x, z, t) = \frac{1}{4\pi^2} \int_{-\infty}^{\infty} \int_{-\infty}^{\infty} \int_{-\infty}^{\infty} \left\{ \hat{p}'_{ex}(k_x, k_z, f) \mathcal{H} \left(\frac{2\pi|f|}{c_\infty + \text{sgn}(f) \mathbf{u}_\infty \cdot \mathbf{k}/k - \Delta u} - k \right) \times e^{i(k_x x + k_z z - 2\pi f t)} \right\} dk_x dk_z df, \quad (10)$$

with

$$\mathbf{k} = (k_x, k_z), \quad k = |\mathbf{k}|, \quad \mathbf{u}_\infty = (U_\infty, 0),$$

where \mathcal{H} is the Heaviside function specified as $\mathcal{H}(q) = 0$, if $q < 0$; $\mathcal{H}(q) = 1$, if $q \geq 0$. The operator, sgn , is the signum function defined as $\text{sgn}(f) = -1$, if $f < 0$; $\text{sgn}(f) = 0$, if $f = 0$; $\text{sgn}(f) = 1$, if $f > 0$. The first term of \mathcal{H} in Eq. (10) gives the upper bound of k for the acoustic domain. Note that the absolute value of the phase velocity is used in this term. The hydrodynamic component is then computed as $p'_{ex,hy} = p'_{ex} - p'_{ex,ac}$.

Define the one-sided space-averaged spectra of \hat{p}'_{ex} as

$$\Psi_{ex}(f) = \frac{2}{L_{gw} W_{gw}} \int_0^{L_{gw}} \int_0^{W_{gw}} |\hat{p}'_{ex}(x, z, f)|^2 dx dz. \quad (11)$$

The space-averaged sound pressure level (SPL) of \hat{p}'_{ex} is calculated by $10 \log [\Psi_{ex}/p_{ref}^2]$.

A preliminary investigation is needed to determine the adjustable parameter Δu . The space-averaged SPLs of \hat{p}'_{ex} and $\hat{p}'_{ex,ac}$ are displayed in Fig. 11, where Δu is set to $0.5U_\infty$, U_∞ , and $1.5U_\infty$. The different values of Δu give converged results. For $\Delta u = U_\infty$, a phase velocity range between 0 m/s and $2U_\infty$ is determined in the streamwise direction. This range is sufficiently wide to involve the main turbulent-flow convection, which has the phase velocity approximately between $0.3U_\infty$ and $1.5U_\infty$, as indicated by the major hydrodynamic domain in Figs. 8 and 9. The acoustic domain defined by \mathcal{H} in Eq. (10) thus includes most of the acoustic energy in the computation of the exterior acoustic component. Hereafter, $\Delta u = U_\infty$ is adopted in the wavenumber-frequency decomposition.

The magnitudes of $\hat{p}'_{ex,ac}$ are much lower than those of \hat{p}'_{ex} , as illustrated in Fig. 11. The acoustic component is a negligible part in the total exterior fluctuating pressure. This phenomenon can be explained based on Lighthill's analogy.^{16,58} The dipole noise and quadrupole noise, which are produced by wall-bounded turbulent flows, scale as Ma_c^3 and Ma_c^4 , where $Ma_c = U_c/c_\infty$ regarding the main convection indicated by the major hydrodynamic domain in Fig. 8. Local peaks of $\hat{p}'_{ex,ac}$ are observed around 1000 Hz and 2000 Hz. The same peak frequencies are also found in the side shear layer and recirculation bubble (see Fig. 5). This suggests that the side shear layer and recirculation bubble are the important sources of the acoustic pressure peaks.

E. Modal analysis of window and cavity

The parameters of several window and cavity modes are given in Table II. The fundamental frequency of the window is 20.2 Hz. For the cavity, the fundamental frequency of the first spatially varying mode is 106.3 Hz. Thus, the window is easier to respond to the exterior dynamic loads at low frequencies below 106.3 Hz in comparison with the cavity.

F. Interior noise

Contours of the interior noise at 100 Hz, 500 Hz, and 1000 Hz, compared to the window and cavity mode shapes, are illustrated in Fig. 12. The distribution of the pressure magnitudes near the window follows the combination of the window and cavity mode shapes. The distribution far away from the window is mainly affected by the cavity mode shapes. The results prove that the responses of the vibro-acoustics system to the exterior excitations are dominated by the structural modes. By contrast, the local features of the exterior flows have a negligible influence on the magnitude distribution of the interior noise.

TABLE II. The information of several window and cavity modes. Here, (i, j, k) represents the numbers of half waves with respect to (x, y, z) of the coordinate system.

	Mode no.	1	2	3	4	5	56	119	251	388
Window	f (Hz)	20.2	37.2	44.8	60.5	64.5	503	998	1994.7	2997.5
	(i, k)	(1, 1)	(2, 1)	(1, 2)	(2, 2)	(3, 1)	(3, 8)	(14, 1)	(1, 17)	(13, 18)
	Mode no.	1	2	3	4	5	60	365	2469	7454
Cavity	f (Hz)	106.3	121.4	141.7	161.4	177.1	501.5	1000.4	2000.1	3000.1
	(i, j, k)	(1, 0, 0)	(0, 0, 1)	(0, 1, 0)	(2, 0, 2)	(2, 2, 0)	(2, 4, 3)	(6, 4, 7)	(10, 12, 7)	(19, 6, 18)

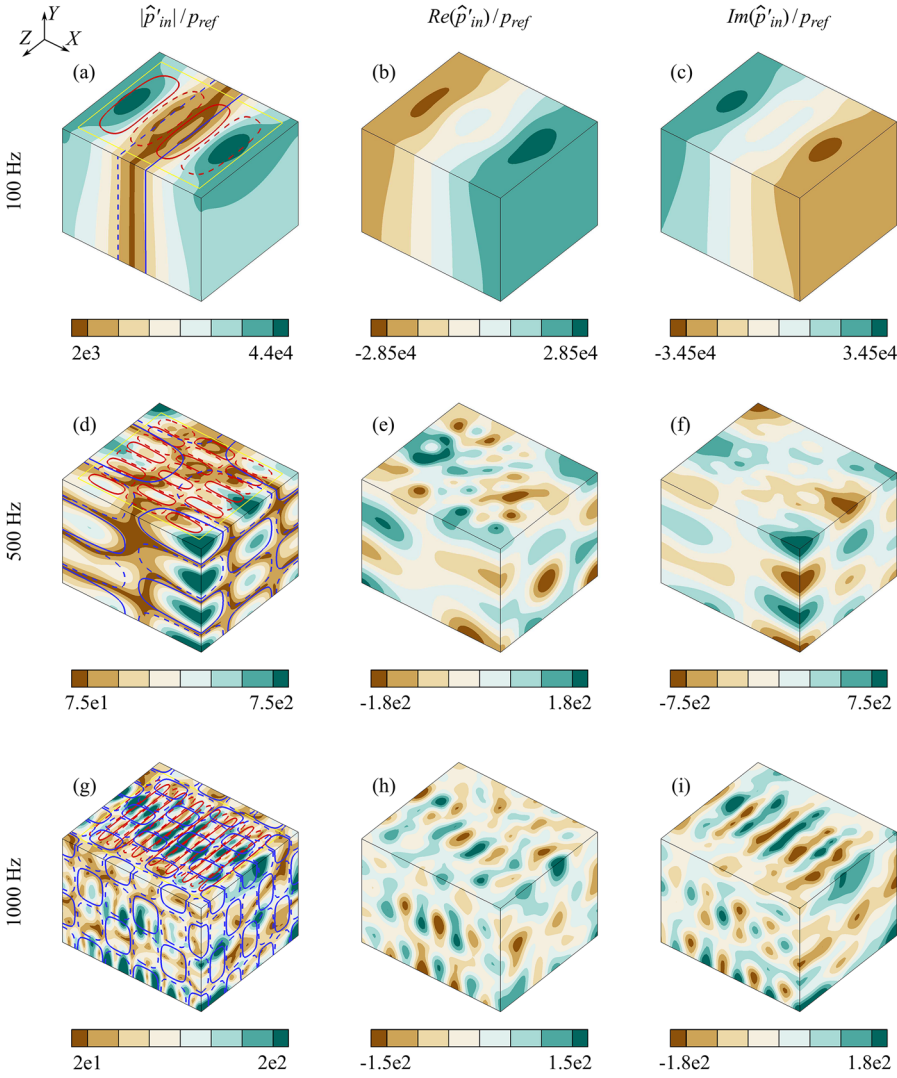


FIG. 12. Contours of the interior noise. From top to bottom, 100 Hz, 500 Hz, and 1000 Hz. From left to right, the magnitudes and real and imaginary parts. The red lines show the window mode shapes at 101.6 Hz, 503 Hz, and 998 Hz; the blue lines show the cavity mode shapes at 106.3 Hz, 501.5 Hz, and 1000.4 Hz. The solid and dashed line patterns represent the normalized mode shape levels of 0.1 and -0.1 , respectively.

The hydrodynamic and acoustic components of the interior noise are predicted based on the corresponding exterior pressure components. The SPLs of the total interior noise and the components at the different positions are shown in Fig. 13. The interior components exhibit apparent local peaks due to the structural resonances. The peak frequencies are observed near the natural frequencies of the window and cavity. This observation suggests that the vibro-acoustic coupling between the two structures is weak. The interior hydrodynamic component is larger than the interior acoustic component below 250 Hz. Therefore, the exterior hydrodynamic component is important in the noise generation at low frequencies. The interior acoustic component becomes predominant above 2000 Hz. This means that the exterior acoustic component dominates the interior noise generation at high frequencies.

To clarify the importance of the interior acoustic component, the space-averaged ratios of this component to the total interior noise are defined by averaging the pressure at the mesh nodes,

$$r_{pin,ac}(f) = \frac{\sum_{q=1}^{N_q} |\hat{p}'_{in,ac}(x_q, y_q, z_q, f)|^2}{\sum_{q=1}^{N_q} |\hat{p}'_{in}(x_q, y_q, z_q, f)|^2}, \quad (12)$$

where N_q is the total number of the nodes in the cavity mesh. The ratios are shown in Fig. 14. Although a few peaks are observed below 250 Hz, the low ratios indicate that the exterior hydrodynamic component plays the dominant role in generation of the interior noise in this low frequency range. The peaks are associated with the resonances, as explained above for the interior SPLs. In terms of the high ratios, it is found that the exterior acoustic component is predominant to generate the interior noise at high frequencies.

The efficiencies of the exterior pressure components can be addressed based on the transmission loss (TL). Define the TL as $TL(f) = 10 \log [\Psi_{ex}(f)/\Psi_{in}(f)]$, where $\Psi_{ex}(f)$ is given in Eq. (11) and $\Psi_{in}(f)$ is given by replacing \hat{p}'_{ex} with \hat{p}'_{in} in this equation. The TLs for the exterior pressure components are displayed in Fig. 15. A negative value is observed for the acoustic component at the fundamental frequency of the window. According to the model by Guy and Bhattacharya,⁵⁹ the negative TL may be related to the mode combination and the condition that the window damping is larger than the air damping. In addition, it could also be caused by the numerical errors in the simulation. The minimum TLs at the fundamental frequency of the window are caused by the resonances. The TLs of the hydrodynamic component are overall much larger than the

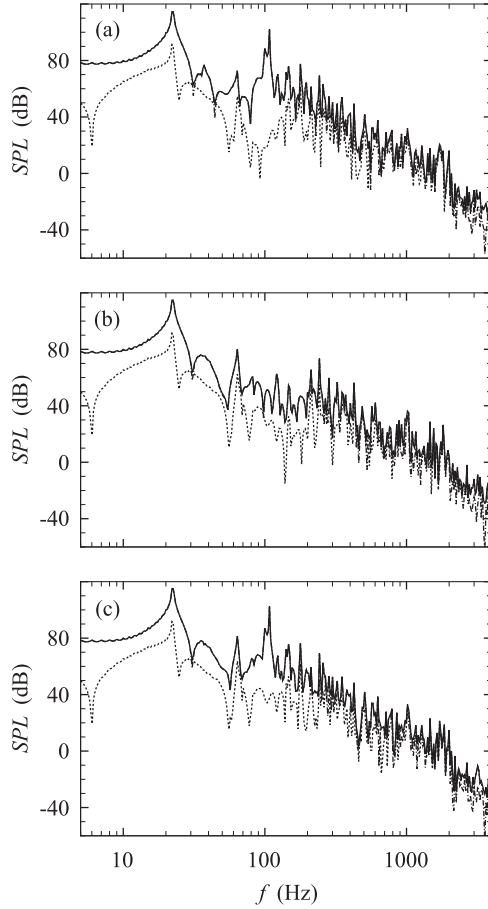


FIG. 13. The SPLs of the total interior noise and its components (a) near the window at $(x, y, z) = (0.2, -0.2, 0.5)$ m, (b) at the cavity center at $(0.8, -0.6, 0)$ m, and (c) near the cavity bottom at $(1.4, -1, -0.5)$ m. The lines depict: —, the total interior noise; ---, the hydrodynamic component; ···, the acoustic component. Note that the hydrodynamic component coincides with the total interior noise below 250 Hz, while the acoustic component coincides with the total interior noise above 2000 Hz.

acoustic component. This means that the hydrodynamic component is less efficient in the interior noise generation than the acoustic component, although it dominates the low-frequency noise generation as discussed above for Fig. 14.

The efficiencies of the exterior pressure components can be explained based on the hydrodynamic and acoustic critical frequencies of the window. The critical frequencies of a flat panel correspond to the smallest coincidence frequencies.⁶⁰

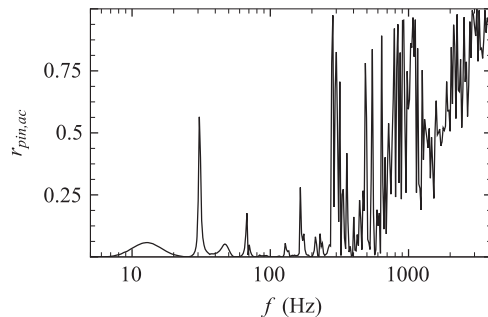


FIG. 14. The space-averaged ratios of the interior acoustic component to the total interior noise.

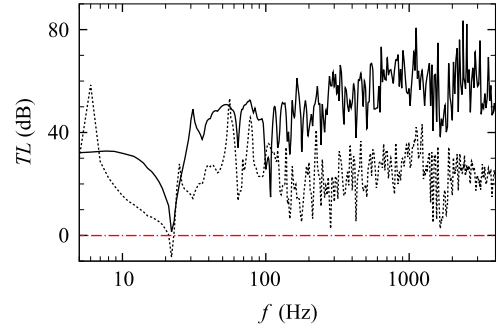


FIG. 15. The TLs: —, the hydrodynamic component; ···, the acoustic component; - - - (red), $TL = 0$.

The components are more efficient near their respective critical frequencies, which have been studied for the TBL (Refs. 13 and 25) and real car mirrors (Ref. 61). The acoustic critical frequency is given by

$$f_{c,ac} = \frac{c_\infty^2}{2\pi h_{gw}} \sqrt{\frac{12\rho_{gw}(1 - \mu_{gw}^2)}{E_{gw}}}. \quad (13)$$

The hydrodynamic critical frequency, $f_{c,hy}$, is defined by replacing c_∞ with U_c in Eq. (13). It is derived that the hydrodynamic and acoustic critical frequencies are 14.9 Hz and 3165.2 Hz, respectively. As displayed in Fig. 15, the hydrodynamic component exhibits an increasing trend of the TLs as the frequencies increase. The high efficiency of this component near the hydrodynamic critical frequency is an important cause of the small TLs at low frequencies, although the minimum TL is found at 21 Hz due to the resonance at the window fundamental frequency. By contrast, the TLs of the acoustic component below 100 Hz are larger than those at high frequencies, and a decaying trend of the TLs is observed above 2000 Hz. The reason of these phenomena is that the acoustic component has the high efficiency near the acoustic critical frequency.

V. CONCLUSIONS

The interior noise in a cuboid cavity, which is induced by turbulent flows past a generic side-view mirror on a plate, is investigated numerically. The cavity is connected to the plate through a rectangular flexible surface that models a 2D glass window. The exterior flows and noise are simulated using a compressible LES method. The window vibration and interior noise are computed by means of a finite element method. A wavenumber-frequency decomposition method is utilized to decompose the exterior surface pressure fluctuations into the hydrodynamic and acoustic components.

It is found that the wake plays an important role in generation of the surface pressure fluctuations. The local characteristics of the wake introduce new features in the wavenumber-frequency spectra of these fluctuations, which cannot be completely explained by the theoretical models of turbulent boundary layers, e.g., the Chase model (Ref. 12). Since the model considers only the streamwise main convection, it can describe a hydrodynamic domain with a regular elliptic distribution in the spectra. However, an

additional minor hydrodynamic domain with a negative convection velocity of $-0.6U_\infty$ is detected in the current spectra. It is caused by the recirculating flow. Another new feature is that the current hydrodynamic domains have elliptic distributions bent with $\pm 12.47^\circ$. The reason is that a spanwise convective expansion happens in the convection.

Due to the resonances, the window modes determine the generation of interior low-frequency tones below 106.3 Hz, which is the fundamental frequency of the spatial varying modes of the cavity. As a result, the lowest transmission losses of the hydrodynamic and acoustic energy are found near the window fundamental frequency (20.2 Hz). The combination of the window and cavity mode shapes strongly affects the distribution of the interior noise magnitudes above 106.3 Hz although the exterior surface pressure fluctuations have the obviously local characteristics.

The exterior acoustic component is generally more efficient to generate the interior noise compared with the exterior hydrodynamic component. However, the hydrodynamic component dominates the generation below 250 Hz. The reason is that this component suffers small transmission losses near the hydrodynamic critical frequency, while the losses increase at high frequencies.

The present study enhances the understanding of the indirect and direct flow-induced interior noise generation by synthesizing the analyses of the exterior flows and noise, the structural vibration, and the interior noise. While a mesh with excessively high resolution can be employed to improve the prediction at high frequencies, we believe that the findings from this study will still be valid. In the future work, it would be interesting to use the dynamic Smagorinsky model since the significant underestimation at high frequencies could result from the extra dissipation produced by the static Smagorinsky model. Another interesting work would be to study the effects of free-stream turbulence on the shear-layer characteristics and reattachment length.

ACKNOWLEDGMENTS

This work has been supported by Fordonsstrategisk Forskning och Innovation (FFI) of VINNOVA—Sweden's innovation agency (Grant No. 2014-01386). The authors offer their appreciation to the Swedish National Infrastructure for Computing (SNIC), who provided computer resources on the cluster Triolith. The authors also offer the appreciation to the reviewers, whose comments have contributed substantially to improve the quality of this study.

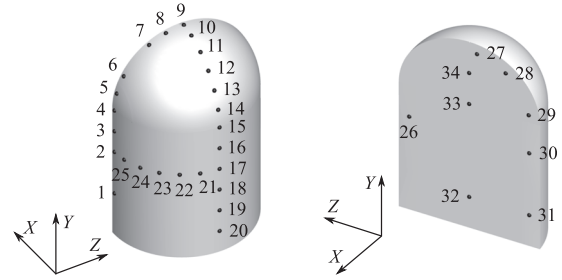


FIG. 17. The locations of the sensors measuring the time-averaged pressure coefficients. The serial numbers of the sensors are labeled.

APPENDIX A: EFFECTS OF WINDOW LOSS FACTOR

In this parametric study, the loss factor of the window, η_{gw} , is set to 0, 0.02, and 0.06. The influences of the factors on the SPLs of the interior hydrodynamic and acoustic components, which are near the window at $(x, y, z) = (0.2, -0.2, 0.5)$ m, are compared in Fig. 16. The different loss factors present the same trends, except for the local minimum and maximum magnitudes due to the resonances. The resonances can be reduced by increasing the loss factors.⁶² Therefore, the assumption of a constant loss factor is believed to be feasible for addressing the principle characteristics of the SPLs.

APPENDIX B: SENSOR LOCATIONS

The sensor locations used to collect the time-average pressure coefficients are shown in Fig. 17. The coordinates of the locations are given in Table III. The detailed experimental settings are presented in the study by Höld *et al.*³¹

APPENDIX C: SPECTRAL ANALYSIS

The Discrete Fourier Transform (DFT) for $p'_{ex}(t)$ is defined as

$$\hat{p}'_{ex}(f_{m_t}) = \frac{1}{N_t} \sum_{j_t=0}^{N_t-1} p'_{ex}(t_{j_t}) \exp(i2\pi f_{m_t} t_{j_t}), \quad (C1)$$

with

$$f_{m_t} = m_t / (N_t \Delta t_s), \quad m_t \in [-N_t/2, N_t/2 - 1],$$

$$t_{j_t} = j_t \Delta t_s, \quad j_t \in [0, N_t - 1],$$

where f_{m_t} denotes the m_t th frequency sample, N_t represents the number of time samples, t_{j_t} is the j_t th sampling instant, and Δt_s is the sampling interval.

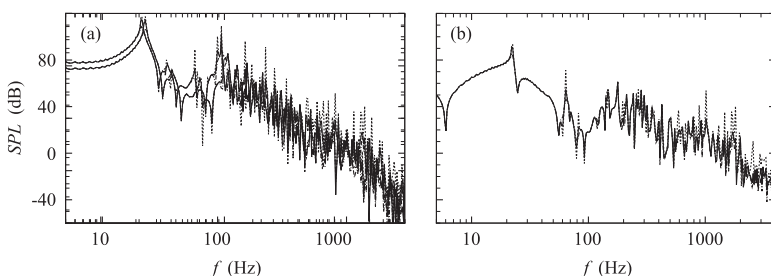


FIG. 16. The SPLs of (a) the interior hydrodynamic component and (b) the interior acoustic component near the window with $(x, y, z) = (0.2, -0.2, 0.5)$ m, computed based on the loss factors: \cdots , 0; $—$, 0.02; $- - -$, 0.06. Note that the lines of the last two loss factors coincide.

TABLE III. The dimensionless coordinates of the sensors,³¹ normalized by D_{mr} .

S1–S3	(0.47, 0.333, −0.499)	(0.47, 0.667, −0.499)	(0.47, 0.833, −0.499)
S4–S6	(0.47, 1, −0.499)	(0.47, 1.129, −0.499)	(0.47, 1.25, −0.432)
S7–S9	(0.47, 1.43, −0.25)	(0.47, 1.482, −0.129)	(0.47, 1.499, 0)
S10–S12	(0.37, 1.483, 0)	(0.25, 1.433, 0)	(0.146, 1.354, 0)
S13–S15	(0.067, 1.25, 0)	(0.017, 1.129, 0)	(0, 1, 0)
S16–S18	(0, 0.833, 0)	(0, 0.667, 0)	(0, 0.5, 0)
S19–S21	(0, 0.333, 0)	(0, 0.167, 0)	(0.017, 0.667, −0.129)
S22–S24	(0.067, 0.667, −0.25)	(0.146, 0.667, −0.354)	(0.25, 0.667, −0.433)
S25–S27	(0.371, 0.667, −0.483)	(0.5, 0.75, 0.425)	(0.5, 1.421, −0.055)
S28–S30	(0.5, 1.337, −0.259)	(0.5, 1.055, −0.421)	(0.5, 0.75, −0.425)
S31–S33	(0.5, 0.25, −0.425)	(0.5, 0.25, 0)	(0.5, 1, 0)
S34	(0.5, 1.25, 0)		

The one-sided power spectral density (PSD) of $\hat{p}'_{ex}(f_{m_t})$ reads

$$\psi_{ex}(f_{m_t}) = 2N_t \Delta t_s \hat{p}'_{ex}(f_{m_t}) \hat{p}'_{ex}(-f_{m_t}), \quad f_{m_t} \geq 0. \quad (C2)$$

Table IV gives the parameters of the signal-processing approach, which are taken to obtain the PSDs in Fig. 5. Here, T denotes the recorded duration and Δf is the frequency resolution. The Butterworth low-pass filter with a cutoff frequency of 2000 Hz is used to process the time samples of the experiments and incompressible simulations. The Hann window is applied as the window function in the present compressible LES. The mean value in every segment of the time samples is subtracted.

For the convenience of understanding the indication of the bandwidth-time product, we consider a signal-processing approach without the window function and the segment overlapping. It can be shown that the sample PSD, $\psi(f)$, of a random signal satisfies the ratio⁶³

$$\frac{\sigma[\psi(f)]}{\psi_{tr}(f)} \approx \frac{1}{\sqrt{BT}} = \frac{1}{\sqrt{(1/T_r)T}} = \frac{1}{\sqrt{\Delta f T}},$$

where σ denotes the standard deviation, $\psi_{tr}(f)$ is the true PSD, B is the resolution bandwidth, and T_r is the duration of every segment. The ratio can be reduced by increasing the bandwidth-time product BT . This indicates that sufficiently large T is required to resolve small B . Thus, the spectra in the present study can be improved by extending the duration of time samples. However, it is observed that the characteristic statistics have been captured as compared with the previous studies (Refs. 30–32).

TABLE IV. The parameters of the signal-processing approach.

	T (s)	Sampling rate (Hz)	Δf (Hz)
Experiments ^{30,31}	0.8	2×10^4	10
Present compressible LES	0.41	1×10^5	9.76
Incompressible DES ³²	0.52	5×10^4	10
Incompressible LES ³²	0.6	5×10^4	10

The spatial-temporal DFT for $p'_{ex}(x, z, t)$ on the window is given by

$$\begin{aligned} \hat{p}'_{ex}(k_{m_x}, k_{m_z}, f_{m_t}) = & \frac{1}{N_x N_z N_t} \sum_{j_x=0}^{N_x-1} \sum_{j_z=0}^{N_z-1} \sum_{j_t=0}^{N_t-1} p'_{ex}(x_{j_x}, z_{j_z}, t_{j_t}) \\ & \times \exp \left[-i \left(k_{m_x} x_{j_x} + k_{m_z} z_{j_z} - 2\pi f_{m_t} t_{j_t} \right) \right], \end{aligned} \quad (C3)$$

with

$$k_{m_x} = 2\pi m_x / (N_x \Delta x_s), \quad m_x \in [-N_x/2, N_x/2 - 1],$$

$$k_{m_z} = 2\pi m_z / (N_z \Delta z_s), \quad m_z \in [-N_z/2, N_z/2 - 1],$$

$$x_{j_x} = j_x \Delta x_s, \quad j_x \in [0, N_x - 1],$$

$$z_{j_z} = j_z \Delta z_s, \quad j_z \in [0, N_z - 1],$$

where k_{m_x} means the m_x th wavenumber sample in the streamwise direction, N_x is the streamwise number of the space samples, x_{j_x} is the j_x th sampling streamwise coordinate, and Δx_s is the streamwise length interval. The same variables in the spanwise direction are represented by k_{m_z} , N_z , x_{j_z} , and Δz_s . The definitions of f_{m_t} , N_t , t_{j_t} , and Δt_s are given in Eq. (C1). The signal-processing approach in the temporal DFT is the same as that in the PSD computation. In the spatial DFT, window functions are not employed.

The normalized wavenumber-frequency spectra are defined as

$$\chi_{ex}(k_{m_x}, k_{m_z}, f_{m_t}) = \frac{|\hat{p}'_{ex}(k_{m_x}, k_{m_z}, f_{m_t})|^2}{\sum_{m_x=-N_x/2}^{N_x/2-1} \sum_{m_z=-N_z/2}^{N_z/2-1} |\hat{p}'_{ex}(k_{m_x}, k_{m_z}, f_{m_t})|^2}. \quad (C4)$$

APPENDIX D: MODAL DENSITIES OF WINDOW AND CAVITY

The modal density, d_{mod} , describes the number of modes contained within a frequency bin of 1 Hz. Since there are limited modes in such a narrow bin width, the density computed based on this bin width would have significant uncertainties. To reduce the uncertainties, the bin width is set to 10 Hz. The center frequencies of the bins are $f = \{20, 30, 40, \dots\}$ Hz. The mode serial numbers and modal density are plotted in Fig. 18.

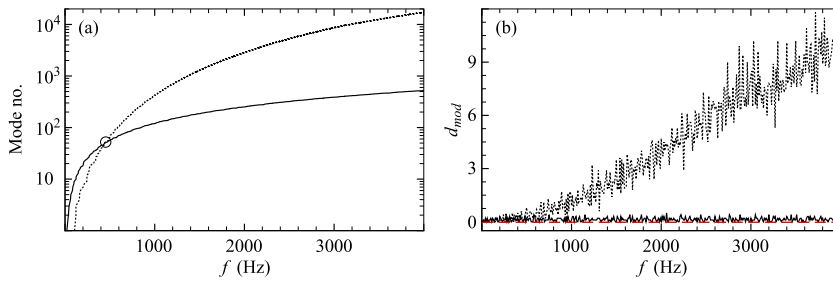


FIG. 18. (a) The mode serial numbers: —, the window; ····, the cavity. The circle marks the frequency of 512.2 Hz, below which both structures have 60 modes. (b) The modal density: —, the window; ····, the cavity; - - - (red), $d_{mod} = 0$.

The window has 10 modes below the cavity fundamental frequency. The modal density of the window changes steadily with the mean value of 0.13. By contrast, the modal density of the cavity increases nonlinearly. Since only the window is found having modes below 106.3 Hz, it dominates the resonances at low frequencies. The high-frequency resonances depend on the combination of the modes of the window and cavity.

- ¹E. Zwicker and H. Fastl, *Psychoacoustics, Facts and Models* (Springer, 1990), pp. 265–269.
- ²A. R. George, “Automobile aerodynamic noise,” SAE Technical Paper No. 900315, 1990.
- ³W. K. Blake, “Fundamentals of flow-induced vibration and noise,” in *Mechanics of Flow-Induced Sound and Vibration, General Concepts and Elementary Sources Vol. 1* (Academic Press, 1986), pp. 288–369.
- ⁴X. Gloerfelt and J. Berland, “Turbulent boundary-layer noise: Direct radiation at Mach number 0.5,” *J. Fluid Mech.* **723**, 318–351 (2013).
- ⁵P. G. Bremner and J. F. Wilby, “Aero-vibro-acoustics: Problem statement and methods for simulation-based design solution,” AIAA Paper 2002-2551, 2002.
- ⁶M. Wang, S. K. Lele, and P. Moin, “Sound radiation during local laminar breakdown in a low-Mach-number boundary layer,” *J. Fluid Mech.* **319**, 197–218 (1996).
- ⁷G. W. He, G. D. Jin, and Y. Yang, “Space-time correlations and dynamic coupling in turbulent flows,” *Annu. Rev. Fluid Mech.* **49**, 51–71 (2017).
- ⁸W. W. Willmarth, “Pressure fluctuations beneath turbulent boundary layers,” *Annu. Rev. Fluid Mech.* **7**, 13–38 (1975).
- ⁹G. W. He, R. Rubinstein, and L. P. Wang, “Effects of subgrid-scale modeling on time correlations in large eddy simulation,” *Phys. Fluids* **14**, 2186–2193 (2002).
- ¹⁰X. Zhao and G. W. He, “Space-time correlations of fluctuating velocities in turbulent shear flows,” *Phys. Rev. E* **79**, 046316 (2009).
- ¹¹D. M. Chase, “Modeling the wavevector-frequency spectrum of turbulent boundary layer wall pressure,” *J. Sound Vib.* **70**, 29–67 (1980).
- ¹²D. M. Chase, “The character of the turbulent wall pressure spectrum at sub-convective wavenumbers and a suggested comprehensive model,” *J. Sound Vib.* **112**, 125–147 (1987).
- ¹³B. Arguillat, D. Ricot, G. Robert, and C. Bailly, “Measured wavenumber: Frequency spectrum associated with acoustic and aerodynamic wall pressure fluctuations,” *J. Acoust. Soc. Am.* **128**, 1647–1655 (2010).
- ¹⁴E. Salze, C. Bailly, O. Marsden, E. Jondeau, and D. Juvé, “An experimental characterisation of wall pressure wavevector-frequency spectra in the presence of pressure gradients,” AIAA Paper 2014-2909, 2014.
- ¹⁵H. D. Yao, G. W. He, M. Wang, and X. Zhang, “Time correlations of pressure in isotropic turbulence,” *Phys. Fluids* **20**, 025105 (2008).
- ¹⁶M. J. Lighthill, “On sound generated aerodynamically. I. General theory,” *Proc. R. Soc. A* **211**, 564–587 (1952).
- ¹⁷C. K. W. Tam, “Intensity, spectrum and directivity of turbulent boundary layer noise,” *J. Acoust. Soc. Am.* **57**, 25–34 (1975).
- ¹⁸Z. Hu, C. L. Morfey, and N. D. Sandham, “Sound radiation in turbulent channel flows,” *J. Fluid Mech.* **475**, 269–302 (2003).
- ¹⁹X. Gloerfelt, “The link between wall pressure spectra and radiated sound from turbulent boundary layers,” AIAA Paper 2010-3904, 2010.
- ²⁰L. Maestrello, “Measurement of noise radiated by boundary layer excited panels,” *J. Sound Vib.* **2**, 100–115 (1965).
- ²¹V. V. Bhat and J. F. Wilby, “Interior noise radiated by an airplane fuselage subjected to turbulent boundary layer excitation and evaluation of noise reduction treatments,” *J. Sound Vib.* **18**, 449–464 (1971).
- ²²W. K. Blake, “Structural response to turbulent wall flow and random sound,” in *Mechanics of Flow-Induced Sound and Vibration, Complex Flow-Structure Interaction Vol. 2* (Academic Press, 1986), pp. 595–657.
- ²³A. O. Borisov and V. T. Grinchenko, “Vibration and noise generation by elastic elements excited by a turbulent flow,” *J. Sound Vib.* **204**, 213–237 (1997).
- ²⁴B. L. Liu, “Noise radiation of aircraft panels subjected to boundary layer pressure fluctuations,” *J. Sound Vib.* **314**, 693–711 (2008).
- ²⁵A. Hekmati, D. Ricot, and P. Druault, “Vibroacoustic behavior of a plate excited by synthesized aeroacoustic pressure fields,” AIAA Paper 2010-3950, 2010.
- ²⁶R. Buchheim, W. Dobrzynski, H. Mankau, and D. Schwabe, “Vehicle interior noise related to external aerodynamics,” *Int. J. Veh. Des.* **3**, 398–410 (1982).
- ²⁷K. Ono, R. Himeno, and T. Fukushima, “Prediction of wind noise radiated from passenger cars and its evaluation based on auralization,” *J. Wind Eng. Ind. Aerodyn.* **81**, 403–419 (1999).
- ²⁸F. Vanherpe, D. Baresh, P. Lafon, and M. Bordji, “Wavenumber-frequency analysis of the wall pressure fluctuations in the wake of a car side mirror,” AIAA Paper 2011-2936, 2011.
- ²⁹M. Hartmann and J. Ocker, “Wind noise caused by the A-pillar and the side mirror flow of a generic vehicle model,” AIAA Paper 2012-2205, 2012.
- ³⁰R. Siegert, V. Schwarz, and J. Reichenberger, “Numerical simulation of aeroacoustic sound generated by generic bodies placed on a plate. Part 2. Prediction of radiated sound pressure,” AIAA Paper 99-1895, 1999.
- ³¹R. Höld, A. Brenneis, A. Eberle, V. Schwarz, and R. Siegert, “Numerical simulation of aeroacoustic sound generated by generic bodies placed on a plate. Part 1. Prediction of aeroacoustic sources,” AIAA Paper 99-1896, 1999.
- ³²J. Ask and L. Davidson, “The sub-critical flow past a generic side mirror and its impact on sound generation and propagation,” AIAA Paper 2006-2558, 2006.
- ³³S. Caro, V. Cotroni, P. Shorter, and F. Mendonça, “Turbulent surface pressure field in low speed flow,” in *Flinovia—Flow Induced Noise and Vibration Issues and Aspects: A Focus on Measurement, Modeling, Simulation and Reproduction of the Flow Excitation and Flow Induced Response*, edited by E. Ciappi, S. D. Rosa, F. Franco, J.-L. Guyader, and S. A. Hambric (Springer, 2013), pp. 91–100.
- ³⁴F. Han, R. J. Bernhard, and L. G. Mongeau, “Prediction of flow-induced structural vibration and sound radiation using energy flow analysis,” *J. Sound Vib.* **227**, 685–709 (1999).
- ³⁵G. Erlebacher, M. Y. Hussaini, C. G. Speziale, and T. A. Zang, “Toward the large-eddy simulation of compressible turbulent flows,” *J. Fluid Mech.* **238**, 155–185 (1992).
- ³⁶H. D. Yao, L. Davidson, and L.-E. Eriksson, “Noise radiated by low-Reynolds number flows past a hemisphere at $Ma = 0.3$,” *Phys. Fluids* **29**, 076102 (2017).
- ³⁷T. A. Zang, R. B. Dahlburg, and J. P. Dahlburg, “Direct and large-eddy simulations of three-dimensional compressible Navier-Stokes turbulence,” *Phys. Fluids* **4**, 127–140 (1992).
- ³⁸C. Wollblad, L.-E. Eriksson, and L. Davidson, “Semi-implicit preconditioning for wall-bounded flow,” AIAA Paper 2004-2135, 2004.
- ³⁹C. Wollblad, L. Davidson, and L.-E. Eriksson, “Large eddy simulation of transonic flow with shock wave/turbulent boundary layer interaction,” *AIAA J.* **44**, 2340–2353 (2006).
- ⁴⁰S. K. Lele, “Compact finite difference schemes with spectral-like resolution,” *J. Comput. Phys.* **103**, 16–42 (1992).
- ⁴¹C. Lator, S. Smirnov, and M. Baelmans, “A finite volume formulation of compact central schemes on arbitrary structured grids,” *J. Comput. Phys.* **198**, 535–566 (2004).

- ⁴²L. E. Eriksson, "Development and validation of highly modular flow solver versions in G2DFLOW and G3DFLOW series for compressible viscous reacting flow," Technical Report 9970-1162, Volvo Aero Corporation, Sweden, 1995.
- ⁴³R. W. Clough and J. Penzien, *Dynamics of Structures* (McGraw-Hill, 1975), pp. 201–215.
- ⁴⁴J.-P. Coyette and J. Manera, "Application of acoustic FEA to the automotive and aircraft industry," SAE Technical Paper 2010-36-0519, 2010.
- ⁴⁵R. J. Astley, G. J. Macaulay, J.-P. Coyette, and L. Cremers, "Three-dimensional wave-envelope elements of variable order for acoustic radiation and scattering. Part I. Formulation in the frequency domain," *J. Acoust. Soc. Am.* **103**, 49–63 (1998).
- ⁴⁶Free Field Technologies (FFT), *Actran 16.0 User's Guide Volume 1: Installation, Operations, Theory and Utilities* (FFT, 2016).
- ⁴⁷M. N. Guddati and B. Yue, "Modified integration rules for reducing dispersion error in finite element methods," *Comput. Methods Appl. Mech. Eng.* **193**, 275–287 (2004).
- ⁴⁸P. R. Amestoy, I. S. Duff, and J.-Y. L'Excellent, "Multifrontal parallel distributed symmetric and unsymmetric solvers," *Comput. Methods Appl. Mech. Eng.* **184**, 501–520 (2000).
- ⁴⁹E. H. Dowell and H. M. Voss, "The effect of a cavity on panel vibration," *AIAA J.* **1**, 476–477 (1963).
- ⁵⁰T. Colonius, S. K. Lele, and P. Moin, "Boundary conditions for direct computation of aerodynamic sound generation," *AIAA J.* **31**, 1574–1582 (1993).
- ⁵¹B. Aloufi, K. Behdinan, and J. Zu, "Vibro-acoustic model of an active aircraft cabin window," *J. Sound Vib.* **398**, 1–27 (2017).
- ⁵²S. Langer and M. Schanz, "Time domain boundary element method," in *Computational Acoustics of Noise Propagation in Fluids—Finite and Boundary Element Methods*, edited by S. Marburg and B. Nolte (Springer, 2008), pp. 495–516.
- ⁵³H. E. Bass, L. C. Sutherland, A. J. Zuckerwar, D. T. Blackstock, and D. M. Hester, "Atmospheric absorption of sound: Further developments," *J. Acoust. Soc. Am.* **97**, 680–683 (1995).
- ⁵⁴F. Ihlenburg, "Finite element error analysis and control for Helmholtz problems," in *Finite Element Analysis of Acoustic Scattering*, Applied Mathematical Sciences Vol. 132 (Springer, 1998), pp. 101–188.
- ⁵⁵E. Kritsikis, M. Aechtner, Y. Meurdesoif, and T. Dubos, "Conservative interpolation between general spherical meshes," *Geosci. Model Dev.* **10**, 425–431 (2017).
- ⁵⁶M. Germano, U. Piomelli, P. Moin, and W. H. Cabot, "A dynamic subgrid-scale eddy viscosity model," *Phys. Fluids A* **3**, 1760–1765 (1991).
- ⁵⁷J. Meyers, B. J. Geurts, and M. Baelmans, "Database analysis of errors in large-eddy simulation," *Phys. Fluids* **15**, 2740–2755 (2003).
- ⁵⁸M. Wang, J. B. Freund, and S. K. Lele, "Computational prediction of flow-generated sound," *Annu. Rev. Fluid Mech.* **38**, 483–512 (2006).
- ⁵⁹R. W. Guy and M. C. Bhattacharya, "The transmission of sound through a cavity-backed finite plate," *J. Sound Vib.* **27**, 207–223 (1973).
- ⁶⁰K. Renji, P. S. Nair, and S. Narayanan, "Critical and coincidence frequencies of flat panels," *J. Sound Vib.* **205**(1), 19–32 (1997).
- ⁶¹B. Neuhierl, S. Senthoooran, R. Toppinga, A. Jäger, M. Brink, T. Lemke, P. Moron, and R. Mutnuri, "From exterior wind noise loads to interior cabin noise: A validation study of a generic automotive vehicle," *SAE Int. J. Passenger Cars: Mech. Syst.* **8**(3), 1075–1081 (2015).
- ⁶²M. P. Norton and D. G. Karczub, "Interactions between sound waves and solid structures," in *Fundamentals of Noise and Vibration Analysis for Engineers*, 2nd ed. (Cambridge University Press, 2003), pp. 193–253.
- ⁶³K. Shin and J. K. Hammond, "Estimation methods and statistical considerations," in *Fundamentals of Signal Processing for Sound and Vibration Engineers* (Wiley, 2008), pp. 317–362.